Lyα in the GJ 1132 System: Stellar Emission and Planetary Atmospheric Evolution

William C. Waalkes[1,*] ⓘ, Zachory Berta-Thompson[1] ⓘ, Vincent Bourrier[2] ⓘ, Elisabeth Newton[3] ⓘ, David Ehrenreich[2] ⓘ,
Eliza M.-R. Kempton[4,5] ⓘ, David Charbonneau[6] ⓘ, Jonathan Irwin[6], and Jason Dittmann[7,†] ⓘ
[1] Department of Astrophysical & Planetary Sciences, 391 UCB 2000 Colorado Avenue, Boulder, CO 80309, USA
[2] Observatoire Astronomique de l'Université de Genève, 51 chemin des Maillettes, 1290 Versoix, Switzerland
[3] Department of Physics and Astronomy, Dartmouth College, Hanover NH 03755, USA
[4] Department of Astronomy, University of Maryland, College Park, MD 20742, USA
[5] Department of Physics, Grinnell College, 1116 8th Avenue, Grinnell, IA 50112, USA
[6] Center for Astrophysics | Harvard-Smithsonian, 60 Garden Street, Cambridge, MA 02138, USA
[7] MIT, 77 Massachusetts Avenue, Cambridge, MA 02139, USA

Abstract

GJ 1132b, which orbits an M dwarf, is one of the few known Earth-sized planets, and at 12 pc away it is one of the closest known transiting planets. Receiving roughly $19\times$ Earth's insolation, this planet is too hot to be habitable but can inform us about the volatile content of rocky planet atmospheres around cool stars. Using Hubble Space Telescope Imaging Spectrograph spectra, we search for a transit in the Lyα line of neutral hydrogen (Lyα). If we were to observe a deep Lyα absorption signature, that would indicate the presence of a neutral hydrogen envelope flowing from GJ 1132b. On the other hand, ruling out deep absorption from neutral hydrogen may indicate that this planet does not have a detectable amount of hydrogen loss, is not losing hydrogen, or has lost hydrogen and other volatiles early in the star's life. We do not detect a transit and determine a 2σ upper limit on the effective envelope radius of $0.36\,R_*$ in the red wing of the Lyα line, which is the only portion of the spectrum we detect after absorption by the ISM. We analyze the Lyα spectrum and stellar variability of GJ1132, which is a slowly rotating 0.18 solar mass M dwarf with previously uncharacterized UV activity. Our data show stellar variabilities of 5%–22%, which is consistent with the M dwarf UV variabilities of up to 41% found by Loyd & France. Understanding the role that UV variability plays in planetary atmospheres is crucial to assess atmospheric evolution and the habitability of cooler rocky exoplanets.

Key words: line: profiles – planets and satellites: atmospheres – planets and satellites: individual (GJ 1132b) – stars: activity – stars: low-mass – ultraviolet: planetary systems

1. Introduction

The recent discoveries of terrestrial planets orbiting nearby M dwarfs (Berta-Thompson et al. 2015; Dittmann et al. 2017; Gillon et al. 2017; Bonfils et al. 2018; Ment et al. 2019) provide us with the first opportunity to study small terrestrial planets outside our solar system, and observatories such as the *Hubble Space Telescope* (*HST*) allow us to analyze the atmospheres of these rocky exoplanets. Additionally, it is important that we learn as much as we can about these planets as we prepare for atmospheric characterization with the *James Webb Space Telescope* (*JWST*; Deming et al. 2009; Morley et al. 2017). *JWST* will provide unique characterization advantages due to its collecting area, spectral range, and array of instruments that allow for both transmission and emission spectroscopy (Beichman et al. 2014).

M dwarfs have been preferred targets for studying Earth-like planets due to their size and temperature, which allow for easier detection and characterization of terrestrial exoplanets. However, the variability and high UV-to-bolometric flux ratio of these stars makes habitability a point of contention (e.g., Shields et al. 2016; Tilley et al. 2019). It is currently unknown whether rocky planets around M dwarfs can retain atmospheres and liquid surface water or if UV irradiation and frequent flaring render these planets uninhabitable (e.g., Scalo et al. 2007; Hawley et al. 2014; Luger & Barnes 2015; Bourrier et al. 2017b). On the contrary, UV irradiation may boost the photochemical synthesis of the building blocks of life (e.g.,

Rimmer et al. 2018). We must study the UV irradiation environments of these planets, especially given that individual M stars with the same spectral type can exhibit very different UV properties (e.g., Youngblood et al. 2017), and a lifetime of UV flux from the host star can have profound impacts on the composition and evolution of their planetary atmospheres.

One aspect of terrestrial planet habitability is volatile retention, including that of water in the planet's atmosphere. One possible pathway of evolution for water on M dwarf terrestrial worlds is the evaporation of surface water and subsequent photolytic destruction of H_2O into H and O species (e.g., Jura 2004; Bourrier et al. 2017b). The atmosphere then loses the neutral hydrogen while the oxygen is combined into O_2/O_3 and/or resorbed into surface sinks (e.g., Wordsworth & Pierrehumbert 2013; Luger & Barnes 2015; Tian & Ida 2015; Shields et al. 2016; Ingersoll 1969). In this way, large amounts of neutral H can be generated and subsequently lost from planetary atmospheres. Studies have shown O_2 and O_3 alone to be unreliable biosignatures for M dwarf planets because they possess abiotic formation mechanisms (Tian et al. 2014), though they are still important indicators when used with other biomarkers (see Meadows et al. 2018). Understanding atmospheric photochemistry for terrestrial worlds orbiting M dwarfs is critical to our search for life.

1.1. Prior Work

Kulow et al. (2014) and Ehrenreich et al. (2015) discovered that Gliese 436b, a warm Neptune orbiting an M dwarf, has a $56.3\% \pm 3.5\%$ transit depth in the blueshifted wing of the

---

Table 1
GJ 1132 System Parameters

Parameter	Value	Source
GJ 1132		
Mass [$M_\odot$]	0.181 ± 0.019	Berta-Thompson et al. (2015)
Radius [$R_\odot$]	$0.2105^{+0.0102}_{-0.0085}$	Dittmann et al. (2017)
Distance [pc]	12.04 ± 0.24	Berta-Thompson et al. (2015)
Radial Velocity [km s^{-1}]	35.1 ± 0.8	Bonfils et al. (2018)
GJ 1132b		
Mass [$M_\oplus$]	1.66 ± 0.23	Bonfils et al. (2018)
Radius [$R_\oplus$]	1.13 ± 0.02	Dittmann et al. (2017)
Semimajor Axis, a [au]	0.0153 ± 0.0005	Bonfils et al. (2018)
Period [days]	1.628931 ± 0.000027	Bonfils et al. (2018)
Epoch [BJD TDB]	$2457184.55786 \pm 0.00032$	Berta-Thompson et al. (2015)
$\frac{a}{R_*}$	$16.54^{+0.63}_{-0.71}$	Dittmann et al. (2017)
i (degrees)	$88.68^{+0.40}_{-0.33}$	Dittmann et al. (2017)
Surface Gravity [m s^{-2}]	12.9 ± 2.2	Bonfils et al. (2018)
Equilibrium Temperature, $T_{\rm eq}$ [K]:		
Bond Albedo = 0.3 (Earth-like)	529 ± 9	Bonfils et al. (2018)
Bond Albedo = 0.75 (Venus-like)	409 ± 7	Bonfils et al. (2018)

stellar Lyα line. Lavie et al. (2017) further studied this system to solidify the previous results and verify the predictions made for the structure of the outflowing gas made by Bourrier et al. (2016). For planets of this size and insolation, atmospheric escape can happen as a result of the warming of the upper layers of the atmosphere, which expand and will evaporate if particles begin reaching escape velocity (e.g., Lammer et al. 2003; Vidal-Madjar et al. 2003; Murray-Clay et al. 2009).

Miguel et al. (2015) find that the source of this outflowing hydrogen is from the H_2-dominated atmosphere of Gl 436b, with reactions fueled by OH^-. Lyα photons from the M dwarf host star dissociate atmospheric H_2O into OH and H, which destroy H_2. H I at high altitudes where escape is occurring is formed primarily through dissociation of H_2 with contributions from the photolyzed H_2O.

Modeling of Gl 436b (Bourrier et al. 2015, 2016) demonstrates that the combination of low radiation pressure, low photoionization, and charge-exchange with the stellar wind can determine the structure of the outflowing hydrogen, which manifests as a difference in whether the light curve shows a transit in the blueshifted region of Lyα or the redshifted region and imprints a specific spectro-temporal signature to the blueshifted absorption. Lavie et al. (2017) used new observations to confirm the Bourrier et al. (2016) predictive simulations that this exosphere is shaped by charge-exchange and radiative braking.

As giant hydrogen clouds have thus been detected around warm Neptunes (see also the case of GJ 3470b; Bourrier et al. 2018a), it opens the possibility for the atmospheric characterization of smaller, terrestrial planets. Miguel et al. (2015) also find that photolysis of H_2O also increases CO_2 concentrations. For Earth-like planets orbiting M dwarfs, understanding the photochemical interaction of Lyα photons with water is very important for the evolution and habitability of a planet's atmosphere.

1.2. GJ 1132b

GJ 1132b is a small terrestrial planet discovered through the MEarth project (Berta-Thompson et al. 2015). It orbits a $0.181\,M_\odot$ M dwarf located 12 parsecs away with an orbital period of 1.6 days (Dittmann et al. 2017). Table 1 summarizes

its basic properties. This is one of the nearest known transiting rocky exoplanets and therefore provides us with a unique opportunity to study terrestrial atmospheric evolution and composition.

While GJ 1132b is too hot to have liquid surface water, it is important to establish whether this planet and others like it retain substantial atmospheres under the intense UV irradiation of their M dwarf host stars. Knowing whether warm super-Earths such as GJ 1132b regularly retain volatiles such as water in their atmospheres constrains parameter space for our understanding of atmospheric survivability and habitability.

Diamond-Lowe et al. (2018) rule out a low mean molecular weight atmosphere for this planet by analyzing ground-based transmission spectra at 700–1040 nm. By fitting transmission models for atmospheric pressures of 1–1000 mbar and varying atmospheric composition, they find that all low mean molecular weight atmospheres are a poor fit to the data, which is better described as a flat transmission spectrum that could be due to a $>10\times$ solar metallicity or $>10\%$ water abundance. Whether these results imply GJ 1132b has a high mean molecular weight atmosphere or no atmosphere at all remains to be seen. If we detect a Lyα transit, then this implies UV photolysis of H_2O into neutral H and O, leading to outflowing neutral H. The oxygen could recombine into O_2 and O_3, resulting in a high mean molecular weight atmosphere, and wholesale oxidation of the surface.

This work serves as the first characterization of whether there is a neutral hydrogen envelope outflowing from GJ 1132b as well as an opportunity to characterize the deepest (longest integration) Lyα spectrum of any quiet M dwarf of this mass.

1.3. Solar System Analogs

The atmospheric evolution and photochemistry we evaluate here is similar to what we have seen in Mars and Venus. Much of Mars' volatile history has been studied in the context of Lyα observations of a neutral H corona that surrounds present-day Mars. Chaffin et al. (2015) use Lyα observations to constrain Martian neutral H loss coronal structure, similar to what we attempt in this work. Indeed, Mars has historically lost H_2O via photochemical destruction and escape of neutral H

(Nair et al. 1994; Zahnle et al. 2008), though the solar wind-driven escape mechanisms for Mars are not necessarily the same as what we propose for GJ 1132b in this work.

Venus has long been the example for what happens when a terrestrial planet is irradiated beyond the point of habitability, as is more than likely the case with GJ 1132b. Venus experienced a runaway greenhouse effect, which caused volatile loss and destruction of H_2O. Kasting & Pollack (1983) study the effects of solar UV radiation on an early Venus atmosphere. They find that within a billion years, Venus could have lost most of a terrestrial ocean of water through hydrodynamic escape of neutral H, after photochemical destruction of H_2O. GJ 1132b has a higher surface gravity than Venus, which would extend this timescale of hydrogen loss, but it also has a much higher insolation, which would reduce the hydrogen loss timescale. Later in this work, we will estimate the expected maximum mass-loss rate for GJ 1132b based on the stellar Lyα profile.

The rest of the paper is organized as follows. In Section 2 we describe the methods of analyzing the Space Telescope Imaging Spectrograph (STIS) data, reconstructing the stellar spectrum, and analyzing the light curves. In Section 3 we describe the transit fit and intrinsic spectrum results. We discuss the results and their implications in Section 4, including estimates of the mass-loss rate from this planet's atmosphere. In Section 5 we describe what pictures of GJ 1132b's atmosphere we are left with.

2. Methods

2.1. Hubble STIS Observations

To study the potential existence of a neutral hydrogen envelope around this planet, we scheduled two transit observations of seven orbits each (two observations several hours from midtransit for an out-of-transit measurement and five observations spanning the transit) with the STIS on the *HST*.[8] We used the G140M grating with the 52 × 0.05 slit, collecting data in TIME-TAG mode with the far-UV (FUV)-MAMA photon-counting detector. This resulted in 14 spectra containing the Lyα emission line (1216 Å), which show a broad profile that has been centrally absorbed by neutral ISM atomic hydrogen.

We reextracted the spectra and corrected for geocoronal emission using the calstis pipeline (Hodge & Baum 1995). The STIS spectrum extraction involved background subtraction, which accounts for geocoronal emission (see Figure 1), leaving us only with the need to model the stellar emission and ISM absorption. We omit data points from both visits that fall within the geocoronal emission signal, wavelengths from both visits that overlapped with strong geocoronal emission and therefore had high photon noise. We thus define our blueshifted region to be $<-60\,\mathrm{km\,s^{-1}}$ and our redshifted region to be $>10\,\mathrm{km\,s^{-1}}$ relative to the star. One potential source of variability is where the target star falls on the slit. If it fell directly on the slit, then the observed flux will be more than if the star was partially off the slit. To account for this, we scheduled ACQ/PEAK observations at the start of each *HST* orbit to center the star on the slit and minimize this variability.

In order to analyze the light curves with higher temporal resolution, we used the STIS time-tag mode to split each of the

14 2 ks exposures into four separate 0.5 ks subexposures. This detector records the arrival time of every single photon, which is what allows us to create subexposures in time-tag mode. Each 2D spectrum subexposure was then converted into a 1D spectrum. To do this, we first defined an extraction window around the target spectrum (see Figure 1) and summed up all the flux in that window along the spatial axis. Extraction windows were also defined on either side of the target in order to estimate the background and subtract that from the target window. This results in a noisy line core but eliminates the geocoronal emission signature (Figure 2(a), (b)). These steps were all performed with calstis.

2.2. Stellar Spectrum Reconstruction

With the same spectra used for light-curve analysis, we created a single weighted average spectrum, representing 29.3 ks (8.1 hr) of integration at Lyα across 14 exposures (Figure 2(c)). This stacked spectrum was used with the LyaPy modeling program (Youngblood et al. 2016) that uses a nine-dimensional MCMC to reconstruct the intrinsic stellar spectrum assuming a Voigt profile. Modeling observed Lyα spectra is tricky because of the neutral ISM hydrogen found between us and GJ 1132. This ISM hydrogen has its own column density, velocity, and line width which creates a characteristic absorption profile within our Lyα emission line.

This model takes three ISM absorption parameters (column density, cloud velocity, and Doppler parameter) and models the line core absorption while simultaneously modeling the intrinsic emission, which would give us the resulting observations. Turbulent velocity of the ISM is assumed to be negligible, with the line width dominated by thermal broadening. A fixed deuterium-to-hydrogen ratio of 1.56×10^{-5} (Wood et al. 2004) is also applied to account for the deuterium absorption and emission near Lyα. Modeling the ISM parameters required us to approximate the local interstellar medium as a single cloud with uniform velocity, column density, and Doppler parameter. While the local ISM is more complex than this single component and contains two clouds (G, Cet) in the line of sight toward GJ 1132 (based on the model described in Redfield & Linsky 2000), our MCMC results strongly favored the velocity of the G cloud, so we defined the ISM priors based on this cloud (Redfield & Linsky 2000, 2008).

We use uniform priors for the emission amplitude and FWHM, and Gaussian priors for the H I column density, stellar velocity, H I Doppler width, and H I ISM velocity. The H I column density and Doppler width parameter spaces were both truncated in order to prevent the model from exploring physically unrealistic values. For $N_{H\,I}$, we restrict the parameter space to 10^{16}–$10^{20}\,\mathrm{cm^{-2}}$, based on the stellar distance (12.04 pc) and typical $n_{H\,I}$ values of 0.01–0.1 cm^{-3} (Redfield & Linsky 2000; Wood et al. 2005). We limit the Doppler width to 6–18 km s^{-1}, based on estimates of the Local Interstellar Cloud (LIC) ISM temperatures (Redfield & Linsky 2000).

2.3. Light-curve Analysis

The extracted 1D spectra were then split into a blueshifted regime and redshifted regime, on either side of the Lyα core (Figure 2(c)) so that we could integrate the total blueshifted and redshifted flux and create four total light curves from the two visits (Figure 5). Each of these light curves was fitted with a

---
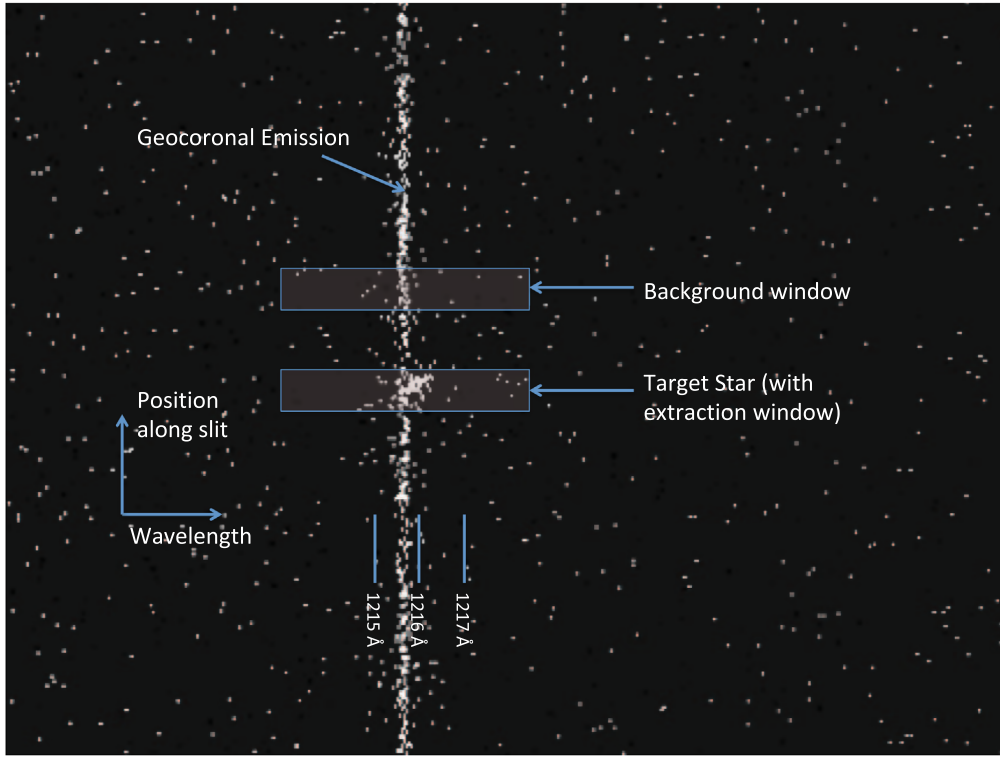
Figure 1. Image of an STIS x2d spectrum. Geocoronal Lyα is shown as a long vertical line while the GJ 1132 Lyα emission is shown in the center.

BATMAN (Kreidberg 2015) light curve using a two-parameter MCMC with the `emcee` package (Foreman-Mackey et al. 2013). The BATMAN models assume that the transiting object is an opaque disk, which is usually appropriate for modeling planetary sizes. However, we are modeling a possible hydrogen exosphere, which may or may not be disk-like, and which would have varying opacity with radius. For this work, we use the BATMAN modeling software with the understanding that our results tell us the effective radius of a cartoon hydrogen exosphere, with an assumed spherical geometry.

We fit for R_p/R_* and the baseline flux using a Poisson likelihood for each visit. We use a Poisson distribution because at Lyα, the STIS detector is receiving very few photons. Our log(likelihood) function is:

$$\ln(\text{likelihood}) = \sum_i [d_i \ln(m_i) - m_i - \ln(d_i!)],$$

where d_i is the total (gross) number of photons detected and m_i is the modeled number of photons detected. The photon model is acquired by taking a BATMAN model of in-transit photons and adding the *sky* photons, which is data provided through the `calstis` reduction pipeline. Uniform priors are assumed for both R_p/R_* and the baseline flux. We restrict our parameter space to explore only effective cloud radii >0, representing physically plausible clouds that block light during transit. By taking simple averages of the light-curve fluxes, we find the ratio of the in-transit flux compared with out-of-transit flux to be 1.01 ± 0.16 for the visit 1 red-wing flux and 0.97 ± 0.13 for the visit 2 red wing. As both are consistent with no detectable transit, the constraints we obtain from the fitting procedure will represent upper limits on the effective size of any hypothetical cloud.

3. Results

3.1. Spectrum Reconstruction

Figure 3 shows the best-fit emission model with 1σ models and a corner plot to display the most crucial modeling parameters, with MCMC results shown in Table 2 and Figure 4. This result gives us the total Lyα flux for this M dwarf.

The results of the stellar spectrum reconstruction indicate that there is one component of Lyα flux that is potentially a result of the low signal-to-noise ratio (S/N) regime of these observations. Additionally, our fit indicates that there is one dominant source of ISM absorption between us and GJ 1132— a single cloud with velocity $-3.1 \, \text{km s}^{-1}$, H I column density $10^{17.9} \, \text{cm}^{-2}$ and Doppler parameter $13.9 \, \text{km s}^{-1}$. Our current understanding of the LIC (Redfield & Linsky 2000, 2008) indicates that there should be two clouds, *G* and *Cet* in the line of sight of GJ 1132, but our derived $v_{\text{H I}}$ is consistent with the velocity of *G*, which is reported as $-2.73 \pm 0.94 \, \text{km s}^{-1}$. We take this to mean that the *G* cloud is the dominant source of absorption and that we can subsequently reconstruct this spectrum under a single-cloud assumption.

By integrating the reconstructed emission profile, we find a Lyα flux of $2.88^{+0.42}_{-0.31} \times 10^{-14} \, \text{erg s}^{-1} \, \text{cm}^{-2}$, which gives $f[\text{Ly}\alpha]/f[\text{bol}] = 2.9 \pm 0.4 \times 10^{-5}$, where we have calculated the bolometric luminosity of GJ 1132b as:

$$f_{\text{bol}} = \sigma T_{\text{eff}}^4 \left(\frac{R_*}{\text{distance}}\right)^2, \tag{1}$$

where values for the T_{eff} and R_* were taken from Bonfils et al. (2018) and the distance to the star is taken from Dittmann et al. (2017). Compared with the Sun, which has $f[\text{Ly}\alpha]/f[\text{bol}] = 4.6 \times 10^{-6}$ (Linsky et al. 2013), we can see that this M dwarf emits fractionally $6\times$ more of its radiation in the ultraviolet.
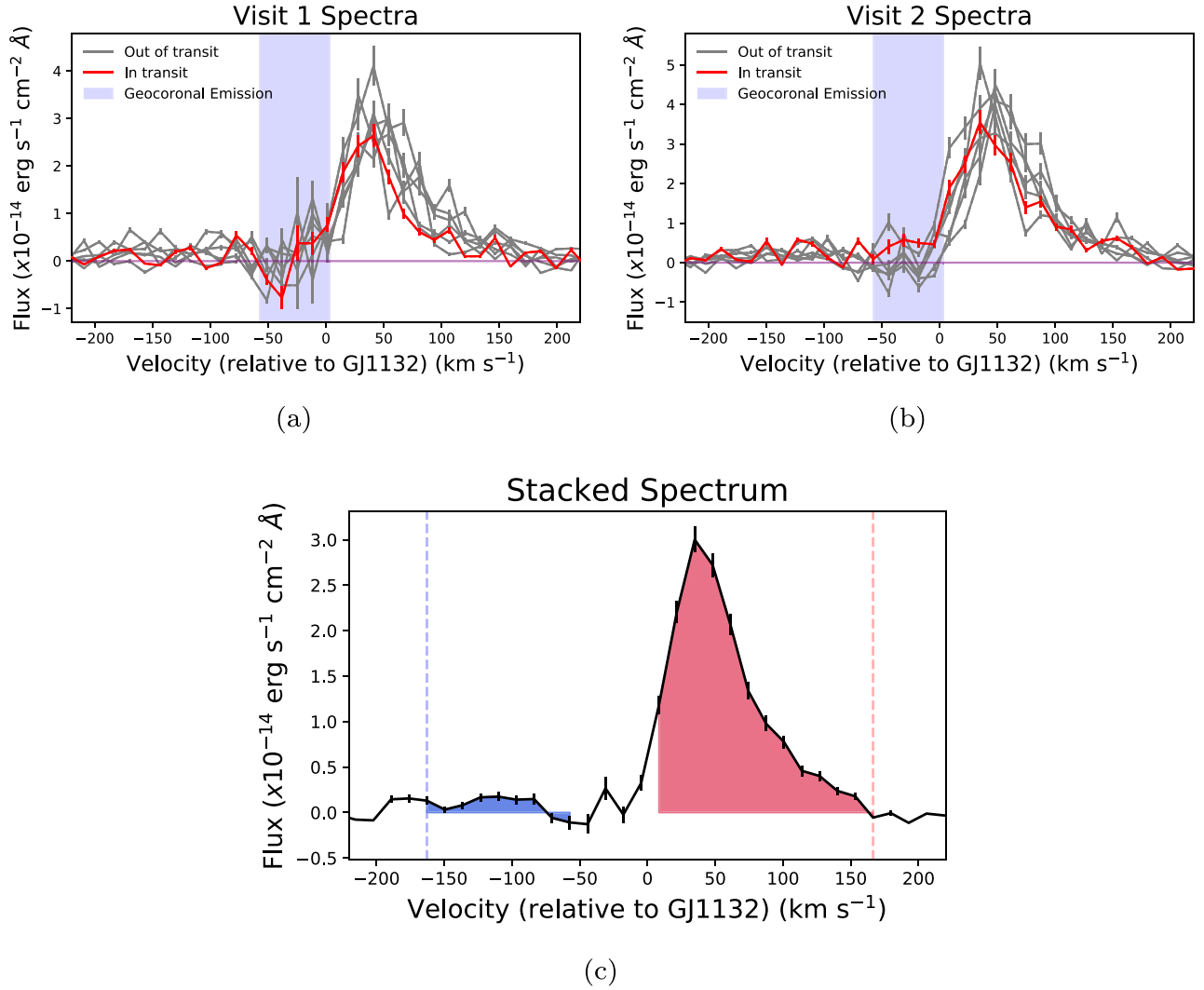
Figure 2. All 14 STIS Lyα spectra in visits 1 (a) and 2 (b) and the averaged stacked spectrum (c). The shape of the stellar Lyα line is a Voigt profile that has been reshaped by convolution with the STIS line spread function and ISM absorption by neutral atomic hydrogen and deuterium. The integration regions for summing up the total Lyα flux are the shaded blue and red areas in (b), with a region in the middle that we omit due to the geocoronal emission. It is apparent that the blueshifted region of the spectrum is at the noise level, and therefore unlikely to give us any viable information. We set the reference velocity for the spectral profiles at 35 km s^{-1}, as this is the cited system velocity (Berta-Thompson et al. 2015).

Table 2
Intrinsic Emission Line Model Parameters Taken from MCMC Samples, with 1σ Error Bars

|	
Line Velocity [km s^{-1}]	$35.23^{+0.99}_{-0.98}$
log(Amplitude) [erg s^{-1} cm^{-2} Å^{-1}]	$-13.23^{+0.08}_{-0.06}$
FWHM [km s^{-1}]	$114.02^{+4.64}_{-4.99}$
log(H I Column Density) [cm^{-2}]	$17.92^{+0.13}_{-0.15}$
Doppler Parameter (b) [km s^{-1}]	$13.91^{+0.74}_{-1.33}$
H I Velocity [km s^{-1}]	$-3.13^{+1.43}_{-1.18}$
Total Flux [erg s^{-1} cm^{-2}]	$2.9 \times 10^{-14+4\times10^{-15}}_{-3\times10^{-15}}$
Total Flux (1 au) [erg s^{-1} cm^{-2}]	$0.18^{+0.03}_{-0.02}$

Note. Total Flux (1 au) is the flux if it were measured 1 au from the star, whereas the Total Flux is the flux as measured at *HST*.

Given the intra-visit stellar variability, we also modeled the average Lyα spectra for visits 1 and 2 separately. All modeled parameters (see Figure 4) were consistent between visits except for

the FWHMs, which were different by 3σ, and the total integrated fluxes, which differed by 2σ ($2.90^{+0.47}_{-0.41} \times 10^{-14}$ erg s^{-1} cm^{-2} for visit 1 and $4.30^{+0.52}_{-0.43} \times 10^{-14}$ erg s^{-1} cm^{-2} for visit 2). For the calculation of mass-loss rates in Section 4.1, we use the integrated flux of the combined reconstructed spectrum (Figure 3).

3.2. Light-curve Modeling

The light curves for both visits are shown in Figure 5. MCMC modeling of these light curves resulted in the best-fit parameters shown in Table 3. We report no statistically significant transits, but we can use the modeling results to calculate limits on the hydrogen cloud parameters. To ensure that we were not biasing our results by converting from the measured flux counts to photons s^{-1}, we also analyzed the flux-calibrated light curves with Gaussian likelihoods based on pipeline errors and found that the results did not significantly differ from what we present here.
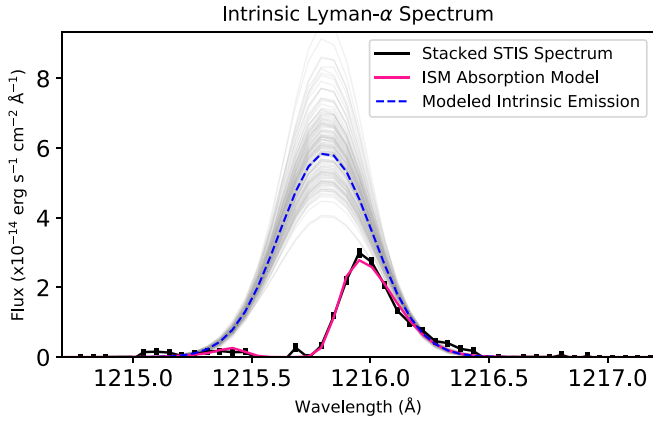
Figure 3. Intrinsic Lyα profile for GJ 1132b, with 200 random MCMC samples in gray. The absorption and intrinsic emission models were modeled with the `Lyapy` software, which assumes a Voigt profile for the emission and parameterizes the ISM absorption into velocity, line width, and column density. Here, the line center is in the system's rest frame.

Table 3
Light-curve Fit Results for MCMC Sampling Where Poisson Likelihoods Were Used

MCMC Results	Visit 1	Visit 2	Joint
R_p/R_* (R)	$0.34^{+0.11}_{-0.15}$	$0.15^{+0.12}_{-0.10}$	$0.22^{+0.09}_{-0.12}$
R_p/R_* (B)	$0.29^{+0.24}_{-0.20}$	$0.46^{+0.30}_{-0.30}$	$0.30^{+0.21}_{-0.21}$
Baseline ($\gamma\,s^{-1}$) (R)	$0.102^{+0.003}_{-0.003}$	$0.136^{+0.003}_{-0.004}$	$0.101^{+0.003}_{-0.003}$ $0.136^{+0.003}_{-0.003}$
Baseline ($\gamma\,s^{-1}$) (B)	$0.013^{+0.001}_{-0.001}$	$0.013^{+0.001}_{-0.002}$	$0.013^{+0.001}_{-0.001}$ $0.013^{+0.001}_{-0.002}$

3.2.1. The STIS Breathing Effect

There is a well-known intra-orbit systematic that shows up in Hubble STIS observations known as the breathing effect, which can result in a change of amplitude of about 0.1% over the course of an *HST* orbit (e.g., Brown et al. 2001; Sing et al. 2008; Bourrier et al. 2017b). This effect is small compared to the photon uncertainty in these observations, but to examine this STIS systematic, we perform our light-curve analysis on the non-time-tagged data. We find that the results are consistent with our time-tagged analysis, so we posit that this effect does not significantly alter our conclusions.

3.3. Stellar Variability

The red wing of our spectral data shows a highly variable stellar Lyα flux over the course of these *HST* visits and we quantify this variability as a Gaussian uncertainty,

$$\sigma_x^2 = \sigma_{\text{measured}}^2 \sigma_{\text{photometric}}^2, \tag{2}$$

where σ_{measured} is our rms noise and $\sigma_{\text{photometric}}$ is the `calstis`-generated error propagated through our spectral integration. Within one 90 minute *HST* orbit, we see flux variabilities (σ_x) of 5%–16% for visit 1 and 7%–18% for visit 2. Among one entire 18-hour visit, variability is 20% for visit 1 and 14% for visit 2 while in the 9 months between the two

visits, there is a 22% offset. These results are consistent with the 1%–41% M dwarf UV variability found by Loyd & France (2014).

4. Discussion

With 14 STIS exposures, we have characterized a long-integration Lyα spectrum and furthered our understanding of the intensity of UV flux from this M dwarf. France et al. (2012) find that as much as half of the UV flux of quiescent M dwarfs is emitted at Lyα, so knowing the total amount of flux at this wavelength serves as a proxy for the total amount of UV flux for this type of star. Figure 7 compares the Lyα flux of GJ 1132 derived in this work compared to other known exoplanet host systems. Our measurement of this Lyα flux provides a useful input for photochemical models of haze, atmospheric escape, and molecular abundances in this planet's atmosphere.

From the redshifted light curves, we can calculate a 2σ upper limit on the radius of this potential hydrogen cloud outflowing from GJ 1132b. We calculate this upper limit (see Figure 6) by taking the joint (visit 1 and visit 2) posterior distributions that resulted from MCMC modeling of these light curves and integrating the CDF to the 95% confidence interval and examining the corresponding R_p/R_*. The 2σ upper limit from the redshifted Lyα spectra gives us an R_p/R_* of 0.36. The upper limit R_p/R_* from the blueshifted light curves is 0.62 but given the very low S/N of that data, this is not a meaningful constraint. The redshifted result is an upper limit on the effective radius of a hydrogen coma, and the real coma could be much more diffuse and asymmetric.

4.1. GJ 1132b Atmospheric Loss

In order to connect our results to an upper limit on the possible mass-loss rate of neutral H from this planet's atmosphere, we follow the procedure outlined in Kulow et al. (2014).

Assuming a spherically symmetric outflowing cloud of neutral H, the equation for mass loss is

$$\dot{M}_{H\,\text{I}} = 4\pi r^2 v(r) n_{H\,\text{I}}(r), \tag{3}$$

where $v(r)$ is the outflowing particle velocity and $n_{H\,\text{I}}(r)$ is the number density of H I at a given radius, r. For this calculation, we will be examining our 2σ upper-limit radius at which the cloud becomes optically thick, where $(R_p/R_*)^2 = \delta = 0.13$. We assume an a$v$ range of 10–100 km s^{-1}, which is the range of the planet's escape velocity (10 km s^{-1}) and the stellar escape velocity (100 km s^{-1}).

Kulow et al. (2014) reduce Equation (3) to

$$\dot{M}_{H\,\text{I}} = \frac{2\delta R_* m v}{\sigma_0} \tag{4}$$

with a Lyα absorption cross-section σ_0 defined as

$$\sigma_0 = \frac{\sqrt{\pi} e^2}{m_e c \Delta \nu_D} f, \tag{5}$$

where e is the electron charge, m_e is the electron mass, c is the speed of light, f is the particle oscillator strength (taken to be 0.4161 for H I), and $\Delta\nu_D$ is the Doppler width, b/λ_0, where we use 100 km s^{-1} for b, as was done in Kulow et al. (2014).

This gives us an upper-limit mass-loss rate of $\dot{M}_{H\,\text{I}} < 0.86 \times 10^9$ g s^{-1} for neutral hydrogen, corresponding to
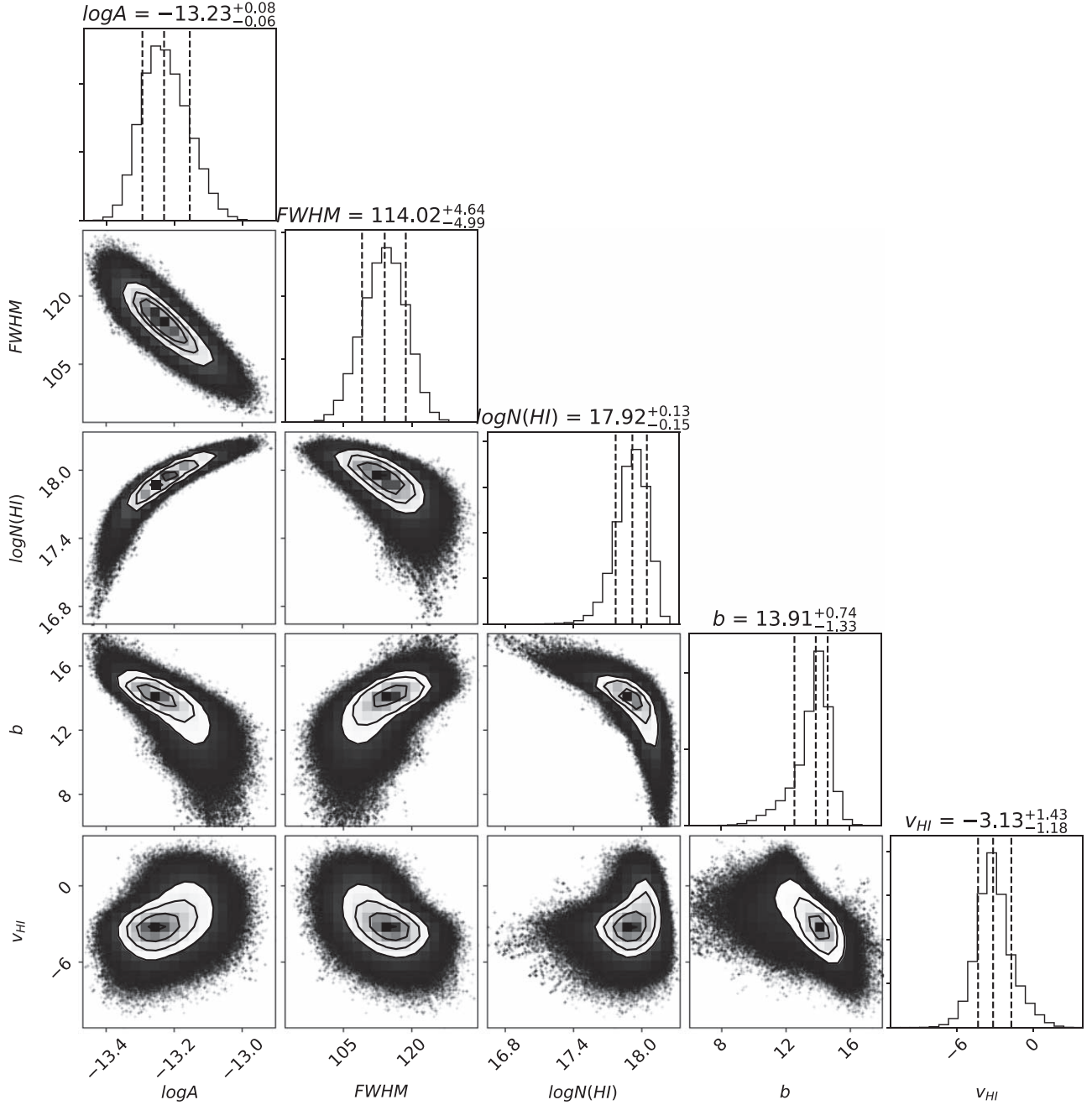
Figure 4. Corner plot showing the samples used in recreating the intrinsic emission profile. We omitted the stellar radial velocity samples because the prior was well constrained by independent radial velocity measurements. In this plot, log(A) is the log of the emission amplitude (which has units of erg s^{-1} cm^{-2} Å^{-1}), FWHM is the emission full width at half maximum in km s^{-1}, log(N(H I)) is the log of the column density of neutral ISM hydrogen (which has units of cm^{-2}), b is the ISM Doppler parameter in km s^{-1}, and v$_{H I}$ is the ISM cloud velocity in km s^{-1}.

15.4×10^9 g s^{-1} of water decomposition, assuming all escaping neutral H comes from H$_2$O. If this upper-limit mass-loss rate was sustained, GJ 1132b would lose an Earth ocean in approximately 6 Myr. If we had actually detected mass loss at this high rate, it would likely indicate that there had been recent delivery or outgassing of water on GJ 1132b, because primordial atmospheric water would have been lost on timescales much shorter than the present age of the system.

We can also calculate the energy-limited mass-loss rate, corresponding to the ratio of the incoming X-ray and ultraviolet (XUV) energy to the work required to lift the particles out of the atmosphere:

$$\dot{M} = \frac{F_{\mathrm{XUV}} \pi R_p^2}{GM_p \, R_p^{-1}} = \frac{F_{\mathrm{XUV}} \pi R_p^3}{GM_p}. \qquad (6)$$

The total F_{XUV} is the flux value at the orbit of GJ 1132b. Using our derived Lyα flux, the Lyapy package calculates stellar EUV spectrum and luminosity from 100 to 1171 Å based on Linsky et al. (2014). From that EUV spectrum, we then calculate the 5–100 Å XUV flux based on relations described in King et al. (2018).

(a)

(b)
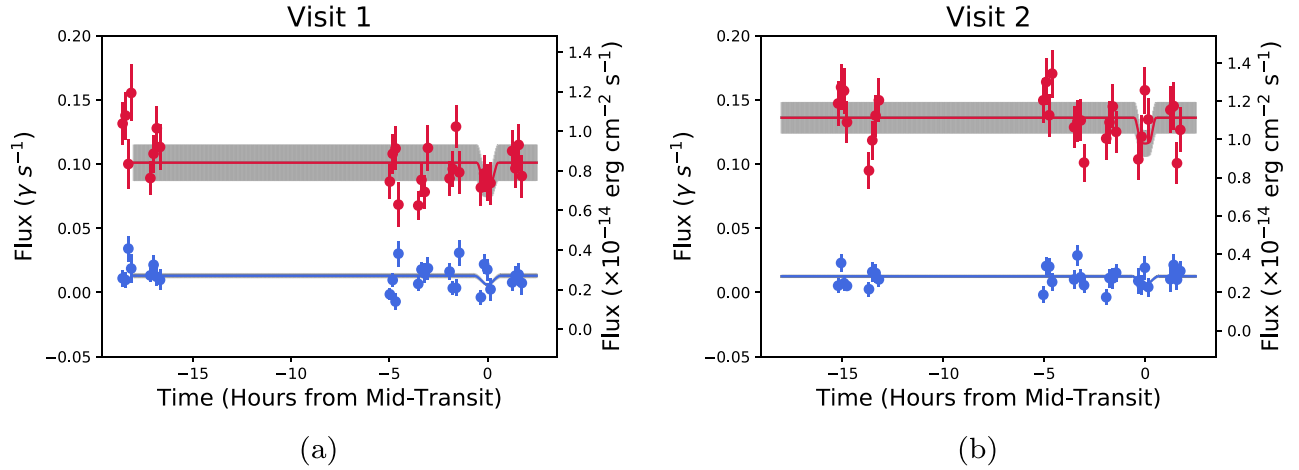
Figure 5. Modeled light curves from both visits. In addition to the calibrated flux values, we display the flux in photons s^{-1} because the S/N is very low at Lyα and this motivated us to use a Poisson likelihood in our analysis of the light curves. Some data points fall to negative values, which can happen when the data point has effectively no flux and then data reduction processes (such as background subtraction) subtract a slightly higher amount of flux. The gray bars indicate what we calculate as a 15% "stellar variability" fudge factor—acquired by calculating what size of error bars would be necessary to result in a χ^2 value of 1 for our best-fit models. The blue wing light curves do not provide much information due to their extremely low flux but we can see from the red wing fits that there is an upper limit on the transit depth.
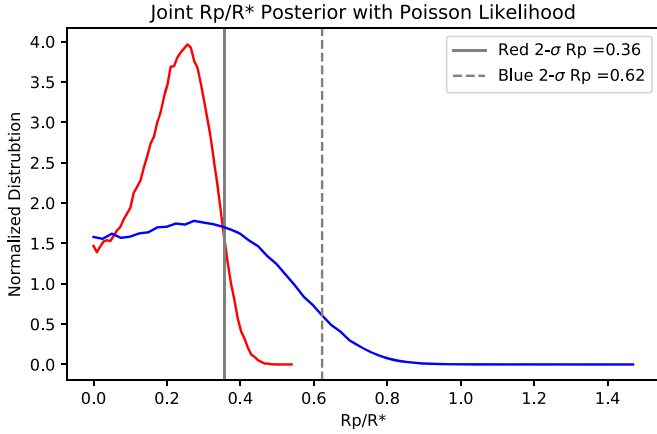
Figure 6. Joint posterior distribution for the R_p/R_* distributions for both visits. Poisson likelihoods were used due to the low photon count regime of these spectra.

Assuming 100% efficiency, we obtain an energy-limited neutral hydrogen mass-loss rate of 3.0×10^9 g s^{-1} estimated from the stellar spectrum reconstruction. This energy-limited escape rate is commensurate with the upper limit we calculate based on the transit depth and stellar properties in the previous section. If we assume a heating efficiency of 1% (based on similar simulations done in Bourrier et al. 2016), then we arrive at a low expected neutral hydrogen loss rate of 3.0×10^7 g s^{-1}, below the level of detectability with these data.

4.2. Simulating H I outflow from GJ 1132b

Figure 8 shows simulation results for neutral hydrogen outflowing from GJ 1132b from the EVaporating Exoplanet code (EVE; Bourrier et al. 2013, 2016). This code performs a 3D numerical particle simulation given stellar input parameters and atmospheric composition assumptions. These simulations were performed using the Lyα spectrum derived in this work, where the full XUV spectrum has been found as described in the previous section. This spectrum is used directly in EVE to calculate the photoionization of the neutral H atoms and calculate theoretical Lyα spectra during the transit of the planet
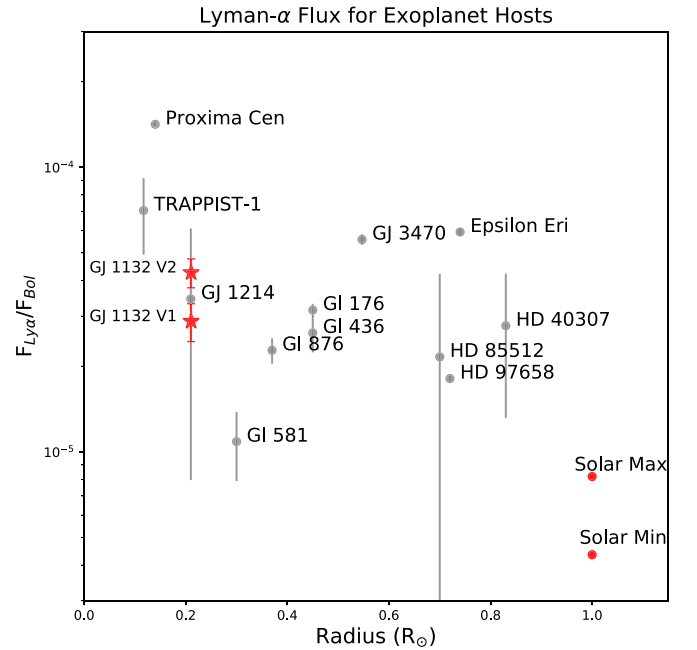

Figure 7. Comparison of $F[\mathrm{Ly}\alpha]/F[\mathrm{bol}]$ for GJ 1132 compared with stars in the MUSCLES Treasury Survey (Youngblood et al. 2016, 2017), TRAPPIST-1 (Bourrier et al. 2017b), HD 97658 (Bourrier et al. 2017a), GJ 436 (Bourrier et al. 2015), GJ 3470 (Bourrier et al. 2018b), as well as the Sun (Linsky et al. 2013). The stars shown here are all M and K dwarfs that are known exoplanet hosts. The error bars on GJ 1132 are statistical errors based on our modeling, so we have included the flux ratios from both visits (9 months apart) to display the variability we see in the data, labeled V1 and V2.

as they would be observed with *HST*/STIS. In addition, our Lyα spectrum is used to calculate the radiation pressure felt by the escaping neutral hydrogen, which informs the dynamics of the expanding cloud.

EVE simulations were created with the following assumptions: the outflowing neutral hydrogen atoms escape from the Roche lobe altitude ($\sim 5\,R_p$) at a rate of 1×10^7 g s^{-1}, modeled as a Maxwellian velocity distribution with upward bulk velocity of 5 km s^{-1} and temperature of 7000 K, resulting in
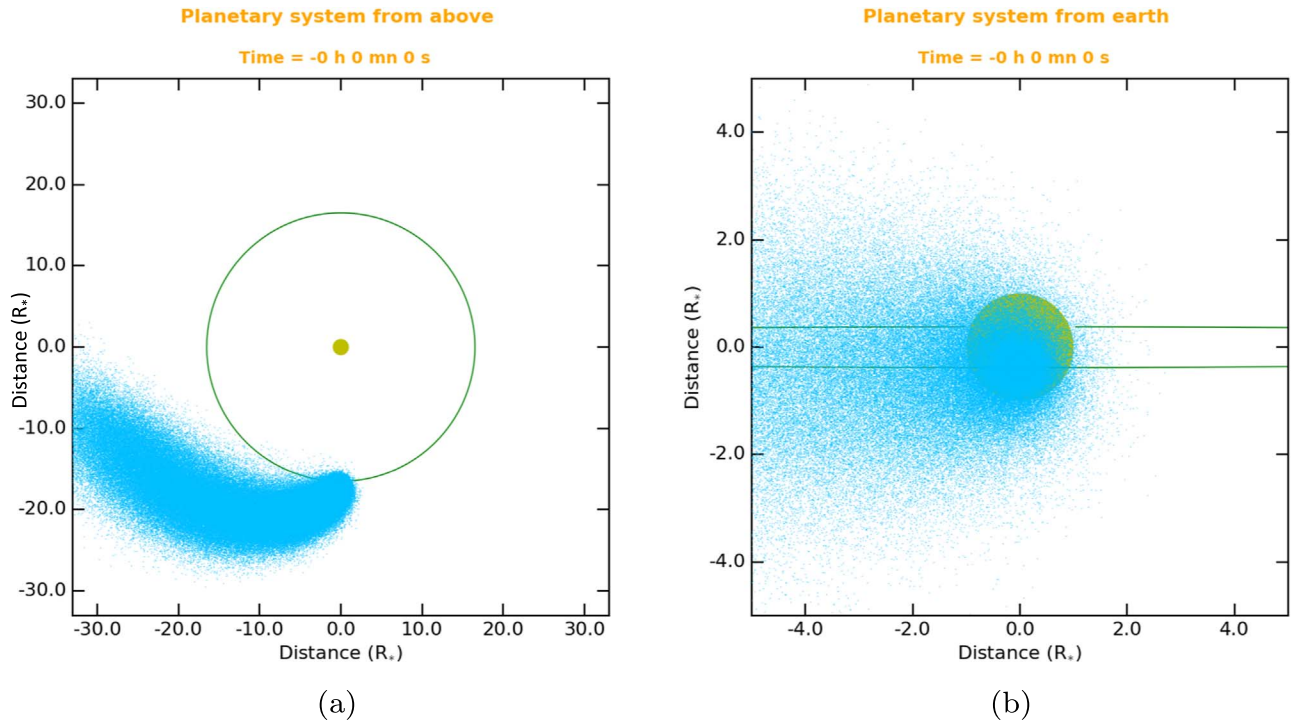
Figure 8. Simulations of the GJ1132 system showing the dynamics of a hypothetical outflowing hydrogen cloud. The left panel shows a top-down view of the system, as a hydrogen tail extends in a trailing orbit. The right panel shows the view from an Earth line of sight, at midtransit.

a cloud that could absorb upwards of 80% of the flux in the blue wing. However, GJ 1132 has a positive radial velocity, so blueshifted flux falls into the regime of ISM absorption and the signal is lost. Simulations of the in-transit and out-of-transit absorption spectra as they would be observed at infinite resolution by *HST* are shown in Figure 9. However, the simulations do not rule out that some thermospheric neutral H may absorb some extra flux in the red wing (see Salz et al. 2016 for a justification of simulation parameters). We note that for planets around M dwarfs, the upward velocity may have a strong influence on the extension of the hydrogen coma. The thermosphere is simulated as a 3D grid within the Roche Lobe, defined by a hydrostatic density profile, and the temperature and upward velocity from above. The exosphere is collisionless with its dynamics dominated by radiation pressure.

There might be other processes shaping the exosphere of GJ 1132b (magnetic field, collisions with the stellar wind, the escaping outflow remaining collisional at larger altitudes than the Roche lobe), but for these simulations we take the simplest possible approach based on what we actually know of the system. Finally, we do not include self-shielding effects of H I atoms within the exosphere, as we do not expect the exosphere is dense enough for self-shielding to significantly alter the results.

The integrated Lyα spectrum corresponds with a maximum ratio of stellar radiation pressure to stellar gravity of 0.4, which puts this system in the regime of radiative breaking (Bourrier et al. 2015), which has a slight effect of pushing neutral hydrogen to a larger orbit. However, the gas is not blown away so the size of the hydrogen cloud will increase if we increase the outward particle velocity. Since the exosphere is not accelerated, most of its absorption is close to $0\,\mathrm{km\,s^{-1}}$ in the stellar reference frame, with some blueshifted absorption because atoms in the tail move to a slightly larger orbit than the planet. This indicates that the lack of blueshifted flux in our
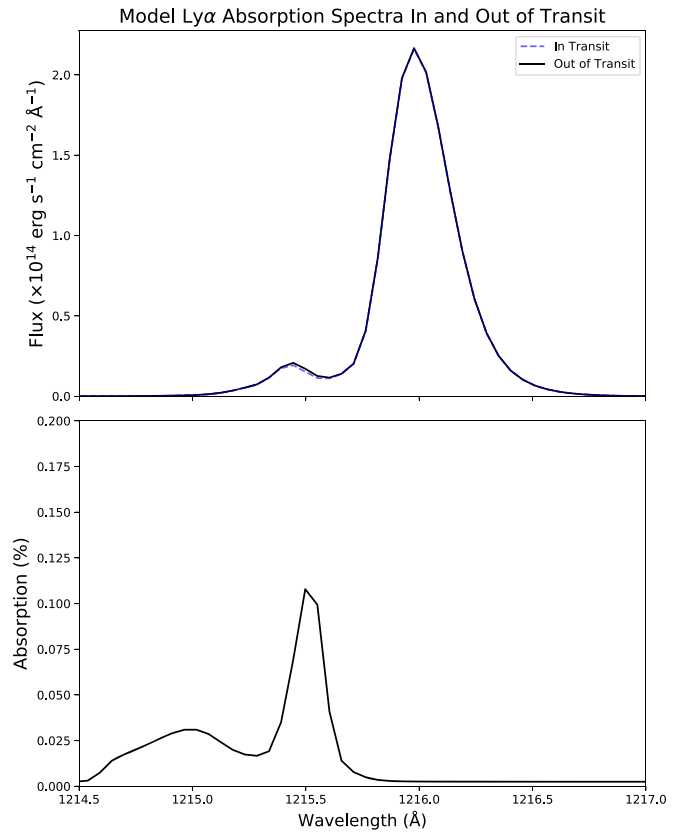
Figure 9. EVE simulated absorption spectra in-transit and 4 hr pre-transit. We can see that the only region of significant absorption is at 1215.5 Å, where absorption peaks at about 12% as seen in the bottom panel. While there is a larger expected flux decrease in the blue wing, the signal is largely in the region that the ISM absorbs and our data are too noisy in the blue wing to detect the possible absorption signal seen in the models. The mass-loss rate corresponding to the above model is $1 \times 10^7\,\mathrm{g\,s^{-1}}$.

9

observations, due to ISM absorption, is a hindrance to fully understanding the possible hydrogen cloud around this planet. The upper-limit cloud size that we quote is based on the observed redshifted flux in a system which is moving away from us at 35 km s^{-1}, so any cloud absorption of flux closer to the line center is outside of the scope of what we can detect.

5. Conclusions

In this work we make the first characterization of the exosphere of GJ 1132b. Until a telescope like LUVOIR (Roberge & Moustakas 2018), these observations will likely be the deepest possible characterization for Lyα transits of this system. If this planet has a cloud of neutral hydrogen escaping from its upper atmosphere, the effective size of that cloud must be less than 0.36 R_* (7.3 R_p) in the redshifted wing. The blue wing indicates an upper limit of 0.62 R_* (12.6 R_p), though this is a very weak constraint. In addition, we were able to model the intrinsic Lyα spectrum of this star.

This Lyα transit's upper limit R_p/R_* implies a maximum hydrogen escape rate of 0.08–0.8 $\times 10^9$ g s^{-1}. If this is the case, GJ 1132b loses an Earth ocean of water between 6 and 60 Myr. Since the mass-loss rate scales linearly with F_{XUV}, we estimate that if this planet were in the habitable zone of its star, about 5× further than its current orbit (based on HZ estimates in Shields et al. 2016), the planet would lose an Earth ocean of water in as little as 0.15–1.5 Gyr. However, these values are based on 2σ upper limits and theoretical calculations suggest mass-loss rates lower than these values, so further Lyα observations are needed to better constrain this mass loss. In addition, these estimates are based on the current calculated UV flux of GJ 1132, which likely decreases over the star's lifetime (e.g., Stelzer et al. 2013) and this results in an underestimate of the mass loss.

The relative Lyα/Bolometric flux is roughly 1 order of magnitude higher for this M dwarf than it is for the Sun, which has grave implications for photolytic destruction of molecules in planets around M dwarfs of this mass. Even when considering the EUV spectrum of GJ 1132 (calculated with methods described in Youngblood et al. 2016) and the EUV flux of the Sun (Zhitnitsky 2018), we find that GJ 1132 emits 6× as much EUV flux (relative to F_{bol}) as the Sun.

This work leaves us with several possible pictures of the atmosphere of GJ 1132b:

1. The real atmospheric loss rates may be comparable to these upper limits, or they may be much less, which leaves us with an open question about the atmosphere and volatile content of GJ 1132b. There could be some loss, but below the detection limit of our instruments.
2. If there is a neutral hydrogen envelope around GJ 1132b, then this super-Earth is actively losing water driven by photochemical destruction and hydrodynamic escape of H. The remaining atmosphere will then be rich in oxygen species such as O_2 and the greenhouse gas CO_2.
3. GJ 1132b could be Mars-like or Venus-like, having lost its H_2O long ago, with a thick CO_2 and O_2 atmosphere remaining, or no atmosphere at all. We posit that this is the most likely scenario, and thermal emission observations with JWST (Morley et al. 2017) would give further insight to the atmospheric composition of GJ 1132b.
4. There might be a giant cloud of neutral hydrogen around GJ1132b based on the EVE simulations, which is

undetectable because of ISM absorption. However, if there are other volatiles in the atmosphere we could detect this cloud using other tracers such as carbon or oxygen with HST in the FUV, or helium (Spake et al. 2018) with ground-based high-resolution infrared spectrographs (see Allart et al. 2018; Nortmann et al. 2018) or with JWST.

GJ 1132b presents one of our first opportunities to study terrestrial exoplanet atmospheres and their evolution. While future space observatories will allow us to probe longer wavelength atmospheric signatures, these observations are our current best tool for understanding the hydrogen content and possible volatile content loss of this warm rocky exoplanet.

ORCID iDs

William C. Waalkes ⬤ https://orcid.org/0000-0002-8961-0352
Zachory Berta-Thompson ⬤ https://orcid.org/0000-0002-3321-4924
Vincent Bourrier ⬤ https://orcid.org/0000-0002-9148-034X
Elisabeth Newton ⬤ https://orcid.org/0000-0003-4150-841X
David Ehrenreich ⬤ https://orcid.org/0000-0001-9704-5405
Eliza M.-R. Kempton ⬤ https://orcid.org/0000-0002-1337-9051
David Charbonneau ⬤ https://orcid.org/0000-0002-9003-484X
Jason Dittmann ⬤ https://orcid.org/0000-0001-7730-2240

References

Allart, R., Bourrier, V., Lovis, C., et al. 2018, Sci, 362, 1384
Beichman, C., Benneke, B., Knutson, H., et al. 2014, PASP, 126, 1134
Berta-Thompson, Z. K., Irwin, J., Charbonneau, D., et al. 2015, Natur, 527, 204

Bonfils, X., Almenara, J.-M., Cloutier, R., et al. 2018, A&A, 613, A25
Bourrier, V., Ehrenreich, D., & des Etangs, A. L. 2015, A&A, 582, A65
Bourrier, V., Ehrenreich, D., King, G., et al. 2017a, A&A, 597, A26
Bourrier, V., Ehrenreich, D., Wheatley, P. J., et al. 2017b, AJ, 154, 121
Bourrier, V., Lecavelier des Etangs, A., Dupuy, H., et al. 2013, A&A, 551, A63
Bourrier, V., Lecavelier des Etangs, A., Ehrenreich, D., et al. 2018a, A&A, 620, A147
Bourrier, V., Lecavelier des Etangs, A., Ehrenreich, D., et al. 2018b, A&A, 620, A147
Bourrier, V., Lecavelier des Etangs, A., Ehrenreich, D., Tanaka, Y. A., & Vidotto, A. A. 2016, A&A, 591, A121
Brown, T. M., Charbonneau, D., Gilliland, R. L., Noyes, R. W., & Burrows, A. 2001, ApJ, 552, 699
Chaffin, M. S., Chaufray, J. Y., Deighan, J., et al. 2015, GeoRL, 42, 9001
Deming, D., Seager, S., Winn, J., et al. 2009, PASP, 121, 952
Diamond-Lowe, H., Berta-Thompson, Z., Charbonneau, D., & Kempton, E. M.-R. 2018, AJ, 156, 42
Dittmann, J. A., Irwin, J. M., Charbonneau, D., et al. 2017, Natur, 544, 333
Ehrenreich, D., Bourrier, V., Wheatley, P. J., et al. 2015, Natur, 522, 459
Foreman-Mackey, D., Hogg, D. W., Lang, D., & Goodman, J. 2013, PASP, 125, 306
France, K., Linsky, J. L., Tian, F., Froning, C. S., & Roberge, A. 2012, ApJL, 750, L32
Gillon, M., Triaud, A. H. M. J., Demory, B.-O., et al. 2017, Natur, 542, 456
Hawley, S. L., Davenport, J. R. A., Kowalski, A. F., et al. 2014, ApJ, 797, 121
Hodge, P., & Baum, S. 1995, Plans for the STScI STIS Pipeline II: Calstis-1, Two-dimensional Image Reduction, STIS Instrument Science Report 95-007
Ingersoll, A. P. 1969, JAtS, 26, 1191
Jura, M. 2004, ApJL, 605, L65
Kasting, J. F., & Pollack, J. B. 1983, Icar, 53, 479
King, P. K., Fissel, L. M., Chen, C.-Y., & Li, Z.-Y. 2018, MNRAS, 474, 5122
Kreidberg, L. 2015, PASP, 127, 1161
Kulow, J. R., France, K., Linsky, J., & Loyd, R. O. P. 2014, ApJ, 786, 132
Lammer, H., Selsis, F., Ribas, I., et al. 2003, ApJL, 598, L121
Lavie, B., Ehrenreich, D., Bourrier, V., et al. 2017, A&A, 605, L7
Linsky, J. L., Fontenla, J., & France, K. 2014, ApJ, 780, 61
Linsky, J. L., France, K., & Ayres, T. 2013, ApJ, 766, 69
Loyd, R. O. P., & France, K. 2014, ApJS, 211, 9

Luger, R., & Barnes, R. 2015, AsBio, 15, 119
Meadows, V. S., Reinhard, C. T., Arney, G. N., et al. 2018, AsBio, 18, 630
Ment, K., Dittmann, J. A., Astudillo-Defru, N., et al. 2019, AJ, 157, 32
Miguel, Y., Kaltenegger, L., Linsky, J. L., & Rugheimer, S. 2015, MNRAS, 446, 345
Morley, C. V., Kreidberg, L., Rustamkulov, Z., Robinson, T., & Fortney, J. J. 2017, ApJ, 850, 121
Murray-Clay, R. A., Chiang, E. I., & Murray, N. 2009, ApJ, 693, 23
Nair, H., Allen, M., Anbar, A. D., Yung, Y. L., & Clancy, R. T. 1994, Icar, 111, 124
Nortmann, L., Pallé, E., Salz, M., et al. 2018, Sci, 362, 1388
Redfield, S., & Linsky, J. L. 2000, ApJ, 534, 825
Redfield, S., & Linsky, J. L. 2008, ApJ, 673, 283
Rimmer, P. B., Xu, J., Thompson, S. J., et al. 2018, SciA, 4, eaar3302
Roberge, A., & Moustakas, L. A. 2018, NatAs, 2, 605
Salz, M., Czesla, S., Schneider, P. C., & Schmitt, J. H. M. M. 2016, A&A, 586, A75
Scalo, J., Kaltenegger, L., Segura, A., et al. 2007, AsBio, 7, 85
Shields, A. L., Ballard, S., & Johnson, J. A. 2016, PhR, 663, 1
Sing, D. K., Vidal-Madjar, A., Désert, J.-M., Lecavelier des Etangs, A., & Ballester, G. 2008, ApJ, 686, 658
Spake, J. J., Sing, D. K., Evans, T. M., et al. 2018, Natur, 557, 68
Stelzer, B., Marino, A., Micela, G., López-Santiago, J., & Liefke, C. 2013, MNRAS, 431, 2063
Tian, F., France, K., Linsky, J. L., Mauas, P. J. D., & Vieytes, M. C. 2014, E&PSL, 385, 22
Tian, F., & Ida, S. 2015, NatGe, 8, 177
Tilley, M. A., Segura, A., Meadows, V. S., Hawley, S., & Davenport, J. 2019, AsBio, 19, 64
Vidal-Madjar, A., des Etangs, A. L., Désert, J.-M., et al. 2003, Natur, 422, 143
Wood, B. E., Linsky, J. L., Hebrard, G., et al. 2004, ApJ, 609, 838
Wood, B. E., Müller, H.-R., Zank, G. P., Linsky, J. L., & Redfield, S. 2005, ApJL, 628, L143
Wordsworth, R. D., & Pierrehumbert, R. T. 2013, ApJ, 778, 154
Youngblood, A., France, K., Loyd, R. O. P., et al. 2016, ApJ, 824, 101
Youngblood, A., France, K., Loyd, R. O. P., et al. 2017, ApJ, 843, 31
Zahnle, K., Haberle, R. M., Catling, D. C., & Kasting, J. F. 2008, JGRE, 113, E11004
Zhitnitsky, A. 2018, PDU, 22, 1